RESEARCH PAPER



Visible light active g-C₃N₄ sheets/CdS heterojunction photocatalyst for decolourisation of acid blue (AB-25)

M. P. Sithole • P. J. Mafa • L.A. de Kock • E. Viljoen • A. T. Kuvarega ©

Received: 1 August 2020 / Accepted: 2 December 2020 / Published online: 4 January 2021 © The Author(s), under exclusive licence to Springer Nature B.V. part of Springer Nature 2021

Abstract Chalcogenide-based semiconductors have attracted research interest due to their potential applications in electronics, energy storage devices, solar cells, and water treatment. In this study, g-C₃N₄ sheets/CdS (CNs/CdS) heterojunction nanocomposites were synthesized using the hydrothermal synthesis method. The CNs/CdS nanocomposites were characterized using field emission scanning electron microscopy (FESEM), transmission electron microscopy (TEM), X-ray diffraction (XRD), Fourier transform-infrared spectroscopy (FTIR), and UV-visible DRS techniques. The FESEM analysis confirmed the formation of CdS wild-berry like structure and successful attachment of CdS to the surface of g-C₃N₄ nanosheets. The PL results indicated reduced rate of electron-hole pair recombination for the 10% CNs/CdS. Upon application of photocatalytic decolourisation of AB-25 with 10% CNs/CdS, there was 99.3% dye removal efficiency achieved after 180 min. The CNs/CdS catalyst was observed to be

This article is part of the topical collection: Nanotechnology Convergence in Africa, Guest Editors: Mamadou Diallo, Abdessattar Abdelkefi, and Bhekie Mamba

M. P. Sithole · P. J. Mafa · L. de Kock · A. T. Kuvarega (☒)

Institute for Nanotechnology and Water Sustainability, College of Science, Engineering and Technology, University of South Africa, Florida Campus, Roodepoort, South Africa e-mail: kuvarat@unisa.ac.za

E. Viljoen

Department of Chemistry, Vaal University of Technology, Private Bag X021, Vanderbijlpark 1900, South Africa stable after 4 repeated cycles, and this could be a pivotal character for real wastewater treatment application by this catalyst.

Keywords Chalcogenide semiconductors · Heterojunction · Photodegradation · Visible light · Water treatment

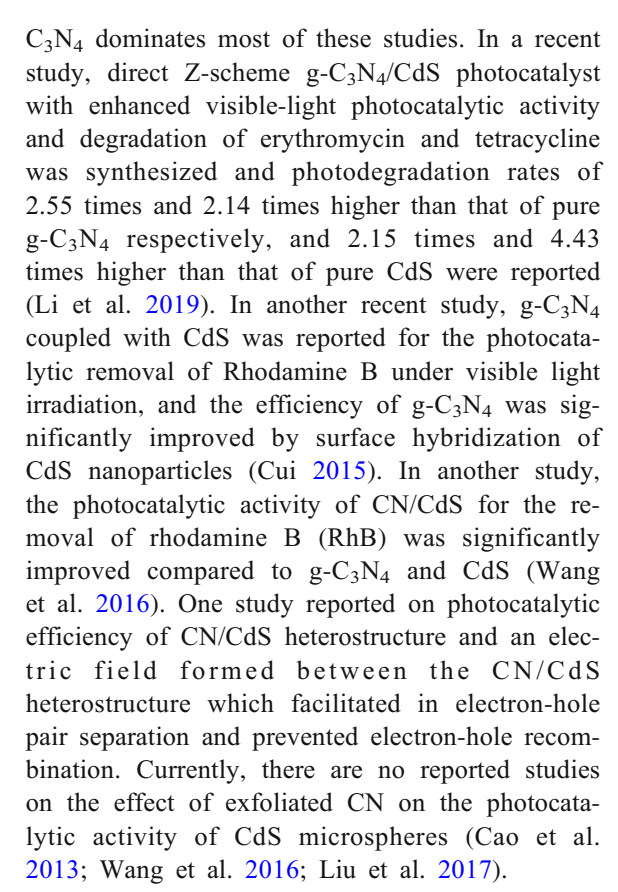
Introduction

Industries are the biggest contributors to water pollution worldwide; they discharge tons of hazardous and toxic chemicals into the water systems. In the past few decades, a large number of new pollutants into the environment have been discovered and most of these pollutants are non-biodegradable and remain in the environment untreated or removed. Partial degradation of these chemicals results in carcinogenic by-products impacting negatively on human health and the ecology (Adeyemo et al. 2012; Baughman and Weber 1994; Liu et al. 2000). Advanced oxidation processes (AOPs) have been widely reported as alternative technologies for the complete removal of these pollutants in water. AOPs are processes that involve the generation of oxidative radicals and potentially mineralize most organic pollutants into non-toxic products (CO₂ and H₂O). Among the semiconductor photocatalysts used, metal oxides such as TiO₂, ZnO, g-C₃N₄, CuO, and CdS have been widely reported as efficient materials for degradation of organic pollutants (Lü et al. 2012; Thompson and Yates 2006; Litter 1999; Bremner et al. 2009). However, these



semiconductors have the drawbacks of low photo-efficiency, high charge carrier recombination and they can only be activated by UV light irradiation (Wang et al. 2014). It is necessary to develop photocatalyst that can utilize solar or visible light energy and result in low recombination of charge carries during photocatalytic applications. Among the many photocatalyst, visible light active chalcogenides such as CdS are promising photocatalyst for removal of organic pollutants in water. CdS has an energy gap of 2.2 eV and it is applicable under visible light activation (El-Hadi and Alamri 2018; Deka et al. 2009; Wu et al. 2012; Yao et al. 2006). The practical use of CdS is still limited by several disadvantages such as high recombination of photo-induced charge carriers and possible photo-corrosion in solution due to the generation of holes under visible light illumination. In addition, CdS nanoparticles tend to agglomerate into larger particles, resulting in high recombination rate of photo induced electrons and holes (Li et al. 2011a; Cao et al. 2013). A number of strategies have been adopted to address these challenges, such as tuning the synthesis methods to produce different dimensional structures (nanoflowers, nanorods, and nanospheres), adding co-catalysts and coupling with other semiconductors (Yao et al. 2006; Ganesh et al. 2017; Lin et al. 2008; Caruso et al. 2001). These interventions are able to promote the separation of charge carriers and improve visible-light activity. The formation of heterostructure through coupling CdS with other semiconductors results in effective separation of electron-holes through formation of an interfacial electric field resulting from the favorable band structures that promote higher photocatalytic activity (Li et al. 2011b; Levchenko et al. 2015; Pal et al. 2016; Pietra et al. 2013).

Recently, graphitic carbon nitride (g- C_3N_4) has attracted lots of interests due to its narrow energy of (2.7 eV) and attractive photocatalytic properties towards visible light applications for water treatment (Kojima and Ohfuji 2018; Wang et al. 2012; Fischer et al. 2008; Wang et al. 2015). It is a metal-free semiconductor, chemically stable and non-toxic (Zou et al. 2016). Recent studies have shown that g- C_3N_4 nanosheets (CNs) compared to bulk g- C_3N_4 (CN) have good properties beneficial for photocatalytic applications such as large specific surface area and enhanced visible light absorption (Senker et al. 2014; Xie et al. 2012). Some studies have reported the application of CN/CdS nanocomposites for wastewater treatment. The effect of CdS on the photocatalytic efficiency of g-



Since the application of heterojunction photocatalysts with uniformly dispersed nanoparticles and strong surface interface is envisaged to enhance the photocatalytic activity of the composite material. Herein, a visible light active heterojunction composite is composed of exfoliated g-C₃N₄ and CdS, which was prepared through an in situ hydrothermal method. The nanocomposite was evaluated for its photocatalytic activity on the decolourisation of Acid blue 25 dye under visible light irradiation.

Experimental

Materials

Cadmium acetate dihydrate (Cd(CH₃COO)₂·2H₂O), thiourea (CH₄N₂S), melamine, sulfuric acid (H₂SO₄), sodium hydroxide, hydrochloric acid, ethanol, benzoquinone, propanol (C₃H₈O), ethylene diamine (C₁₀H₁₆N₂O₈), and AB-25 were all purchased from Sigma-Aldrich (South Africa) and were used without



further purification. Deionized water was used throughout this research study.

Preparation of g-C₃N₄ nanosheets

Bulk g-C₃N₄ (CN) was prepared by polymerization of melamine at 550 °C at a heating rate of 10 °Cmin⁻¹ for 6 h in a furnace. The resultant yellow agglomerate was crushed into fine powder. The bulk g-C₃N₄ (0.5 g) was added to 15 mL concentrated H₂SO₄ (98 wt.%) in a 200 mL beaker and stirred for 10 min. 10 mL deionized water was added rapidly to the yellow suspension with vigorous stirring until it turned into a colorless transparent solution. 150 mL ethanol was then added to form a white precipitate. The precipitate was centrifuged and washed using ethanol and deionized water, then dried at 60 °C for 24 h, and calcined at 400 °C for 1 h. The resulting g-C₃N₄ sheets were labeled CNs.

Synthesis of g-C₃N₄ sheets/CdS (CNs/CdS) nanocomposite

CNs/CdS nanocomposites were prepared via the hydrothermal method. Briefly, 2.3 g of Cd(CH₃COO)₂·2H₂O and 0.36 g of CH₄N₂S was dissolved in 60 ml deionized water and stirred for 1 h. Thereafter, 10%, 20%, and 30% CNs were added to the solution and stirred for 24 h to achieve a homogeneous suspension; the resulting solution was transferred into a steel autoclave and then heated at 180 °C for 24 h. The resulting orange solid sample was centrifuged and washed using ethanol and deionized water to remove impurities before drying.

Photocatalytic evaluation

The photocatalytic decolourisation of acid blue (AB) dye was carried out under visible light irradiation using a 24 V RGB LED (100% intensity) light source, consisting of a glass beaker (V = 2 L) wrapped up by 5 m LED strip (white color; 12 W.m⁻² power rating) externally coated by aluminum foil for control of external light (Fig. 1). The photocatalyst (20 mg) was added to 50 mL of AB dye (20 mg L⁻¹) solution. The dye solution was magnetically stirred for 30 min in the absence of light to achieve equilibrium. The LED light was then switched on and 3 mL aliquots were withdrawn at 30 min time intervals and 0.45 μ m PVDF membrane filter was used to filter any catalyst withdrawn with the solution. The dye aliquots at maximum

wavelength of 603 nm were analyzed using UV-visible spectrophotometry. The photocatalytic removal (PR) of the dye was evaluated using Eq. (1);

$$PR(\%) = (1 - C_t/C_0) \times 100\% \tag{1}$$

where C_0 and C_t are the concentrations of the pollutant at t = 0 and t = t, respectively.

Characterization

FTIR analysis was performed using a PerkinElmer FTIR spectrometer Frontier (spectrum 100 spectrometer) in the range of 400–4500 cm⁻¹. The X-ray diffraction (XRD) patterns were determined using a Rigaku SmartLab X-Ray Diffractometer at room temperature using the Cu-K

 $(\lambda = 0.154059 \text{ nm})$ source operated at 45 kV and 200 mA with 2θ range of 10° to 90° and scan speed of 2° min⁻¹. The optical properties were determined using diffuse reflectance UV-Vis absorption spectrophotometry on a PerkinElmer UV/Vis/NIR spectrometer Lambda 1050. Surface morphologies and elemental composition of the materials were investigated with JEOL JSM-7800F field emission scanning electron microscope (FESEM) coupled with Thermo Scientific Ultradry EDS detector. The surface area was evaluated on an Emmett-Teller (BET) using Micrometrics Trista II surface area and porosity analyzer; the samples were degassed at 180 °C for 12 h using a Micrometrics VacPrep 061 sample degassing system. Photoluminescence spectra were obtained on a HORIBA Fluorolog 3 (FL-1057) using 450 W tungsten xenon lamps as the excitation source at a wavelength of 350 nm and 372 nm.

Results and discussion

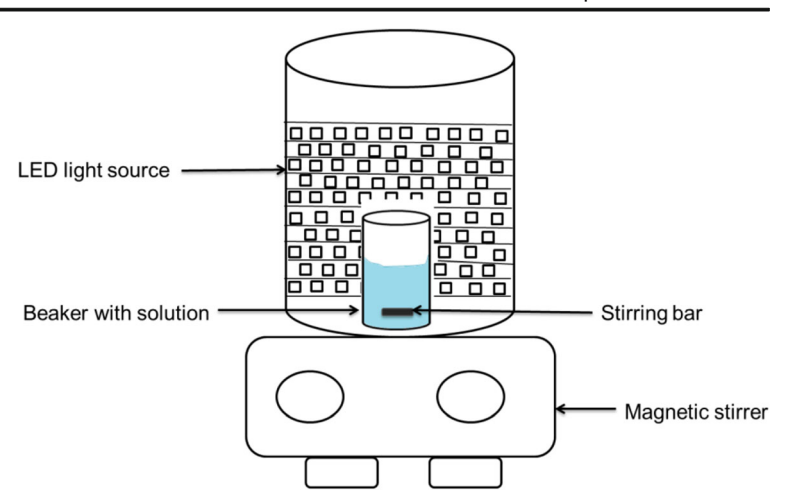
XRD and FTIR analysis

The crystalline phases of CN and CNs and (10%, 20%, and 30%) CNs/CdS were characterized using XRD technique (Fig. 1a). The characteristic peaks of CN were observed at 2θ of 12.8° and 27.5°, and these are indexed to (100) and (002) planes corresponding to structural packing motif of tri-s-triazine units and interplanar stacking of CN according to JCPDS No. 87–1526. In CNs; those peaks down-shifted to 12.2° and 27.3° due to chemical exfoliation (Jiang et al. 2014; Vadivel et al. 2016). The distinct peaks of CdS were centered at 24.8°,



16 Page 4 of 17 J Nanopart Res (2021) 23: 16

Fig. 1 Schematic diagram of a custom made LED photoreactor



26.5°, 28.2°, 43.8°, 47.9°, and 52.9° according to JCPDS No. 41–1487 (Jiang et al. 2014; Vadivel et al. 2016; Rengaraj et al. 2010). These peaks are indexed to (100), (002), (101), (110), (103), and (112) crystal planes of the hexagonal wurtzite structure of CdS. For CNs/CdS composites, CdS maintained its crystallinity and the (002) peak intensity was reduced due to the interaction of the two materials.

The crystallite sizes (d) and micro-strain (ϵ) of the prepared materials were estimated using Eqs. (2) and (3);

$$d = 0.9\lambda/\beta\cos\theta\tag{2}$$

$$\varepsilon = \beta/4 \tan \theta \tag{3}$$

where λ is Cu-K radiation wavelength (0.154059 nm), β is the full width at half maximum (FWHM) in radians, and θ is the Bragg angle. The calculated crystallite size and micro-strain values of CN, CNs, CdS, 10%, 20%, and 30% CNs/CdS are listed in Table 1. The crystallite size of CN got reduced when exfoliation process was performed, and the micro-strain increased. This could be attributed to the presence of S intercalates during chemical exfoliation. As it can be observed, the crystallite size of CdS decreased with an increasing amount of CNs, while the micro-strain values increased with an increase in the quantity of CNs. The change in the micro-strain indicates that the crystalline structure of the material changed slightly while its d-spacing remained unchanged.

FTIR was used to determine the functional groups of the prepared materials as shown in Fig. 1b. The FTIR spectrum of CN and CNs are almost similar except that the peaks in CNs are much reduced. The sharp at 807 cm⁻¹ is ascribed to the tri-s-triazine ring. The bands

in the region 1200-1700 cm⁻¹ are ascribed to the stretching modes of trigonal N(-C)₃ or bride of C-NH-C and C=N units, and these peaks in CNs are slightly shifted probably due to the protonation and disintegration of CN. The broad bands between 3100 and 3500 cm⁻¹ are ascribed to O-H and the terminal amino groups, respectively (Zou et al. 2016; Cote et al. 2009; Zhou et al. 2015). As for pure CdS, there are four characteristic peaks observed at 3452, 1641, 1392, and 1117 cm⁻¹, respectively. The peaks at 3452 and 1641 cm⁻¹ are ascribed to the adsorbed water molecules on the surface of CdS, while the peaks at 1391 and 1117 cm⁻¹ can be indexed to the Cd-S bond, which indicates successful formation of CdS (Fu et al. 2013). For the composite materials, the IR band characteristics of CNs and CdS are observed, confirming that the composite materials were composed of both CNs and hexagonal CdS.

Table 1 The d-spacing, crystalline size, and micro-strain of the as-prepared materials

Sample	d-spacing (nm)	Crystallite size (nm)	Micro- strain
CN	0.324	19.05	0.0019
CNs	0.326	14.99	0.0026
CdS	0.358	71.84	0.0006
10% CNs/CdS	0.336	58.47	0.0009
20% CNs/CdS	0.336	60.24	0.0009
30% CNs/CdS	0.336	44.88	0.0012



Morphology and chemical structure analysis

The morphology and elemental compositions of the materials were studied using FESEM (Fig. 2). The morphology of CN appeared agglomerated with irregular micrometer size block and small pores resulting from the gas discharged when melamine was decomposed (Fig. 2a) (Tang et al. 2016). Bulk CN was chemically exfoliated and layered smooth sheet-like material was obtained (Fig. 2b) (Vadivel et al. 2016; Xu et al. 2013). CdS displayed the berry-like morphology in the microrange scale and the material showed minimum aggregation berry-like flowers (Fig. 2c). As shown in Fig. 2d–f, the CdS berry-like well scattered and embedded on CNs surface, symbolizing the interaction between CNs and CdS. Figure 2d, e displaced strong attachment between the two materials, and this could be helpful for photocatalytic activities. However, as the CNs quantity was further increased to 30%, there was distortion observed on CNs and most of the CdS material were scattered unattached to CNs. This could be not favorable for photocatalytic decolourisation of AB-25 (Fig. 3).

The EDS spectrum of the CNs confirmed the presence of C, N, O, and S (Fig. 4a). The small S peak was due to residual H_2SO_4 used for exfoliation of the CN. The 10% CNs/CdS composite revealed the presence of C, O, N, Cd, and S elements (Fig. 4b) as was anticipated. The C and N peaks were subdued due to the amounts of CdS used in the synthesis. The presence of these elements confirmed the successful preparation of CNs/CdS

materials with an interface that could be pivotal to the process of photocatalytic decolourisation.

The TEM morphology of CdS, CNs, and 10% CNs/CdS is shown on (Fig. 5a-c). Figure 5a shows a low magnification bright-field TEM image of the CdS image. The TEM image of the CdS surface-displayed small particle-like materials and this is consistent with the FESEM results. The TEM image also shows that CN was successfully exfoliated to ultra-thin sheets (Fig. 5b). Furthermore, the TEM image of 10% CNs/CdS nanocomposite shows two morphologies, lighter sheet-like structure that are almost transparent, ascribed to CNs and the darker plate-like morphology, ascribed to CdS confirming formation of CdS and CNs interface (Fig. 5c). A closer look at the interface of the two materials showed the distinct interface region between the two different materials (CNs and the CdS).

BET analysis

The specific surface areas and pore volumes of the synthesized materials were obtained by the Brunauer-Emmett-Teller (BET) as displayed in Fig. 6. It can be observed that the samples showed type IV adsorption-desorption isotherms with type H3 hysteresis loops (Mafa et al. 2020a). This shows the formation of slit-shaped pores with plate-like particles and can be attributed to the presence of mesopores in the samples (Mafa et al. 2020b). As shown in Table 2, the BET surface areas of CN, CNs, CdS, and 10% CNs/CdS materials

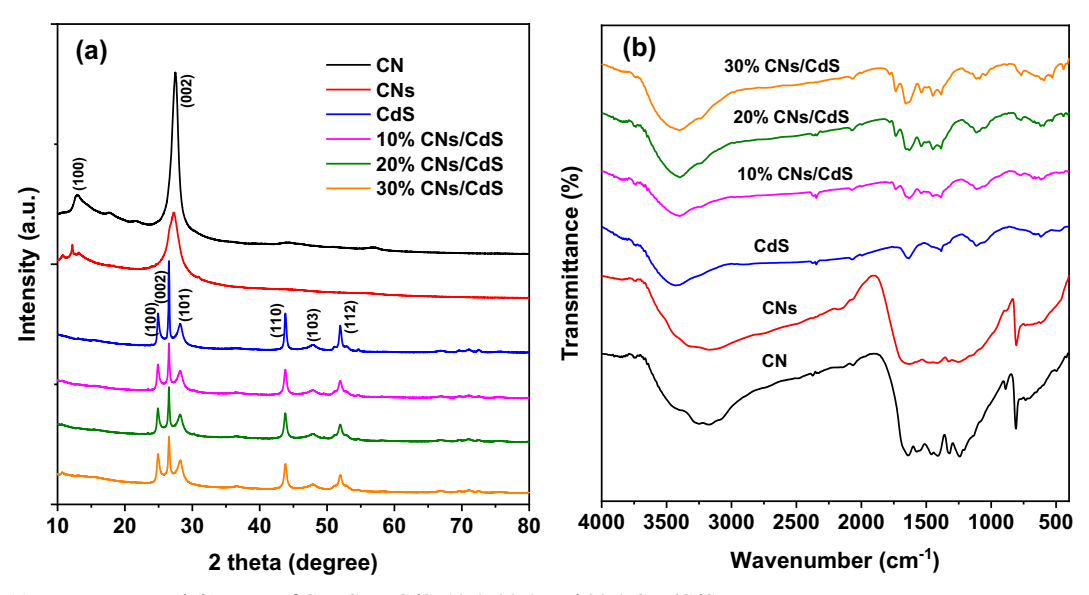


Fig. 2 (a) XRD pattern and (b) FTIR of CN, CNs, CdS, 10%, 20%, and 30% CNs/CdS



16 Page 6 of 17 J Nanopart Res (2021) 23: 16

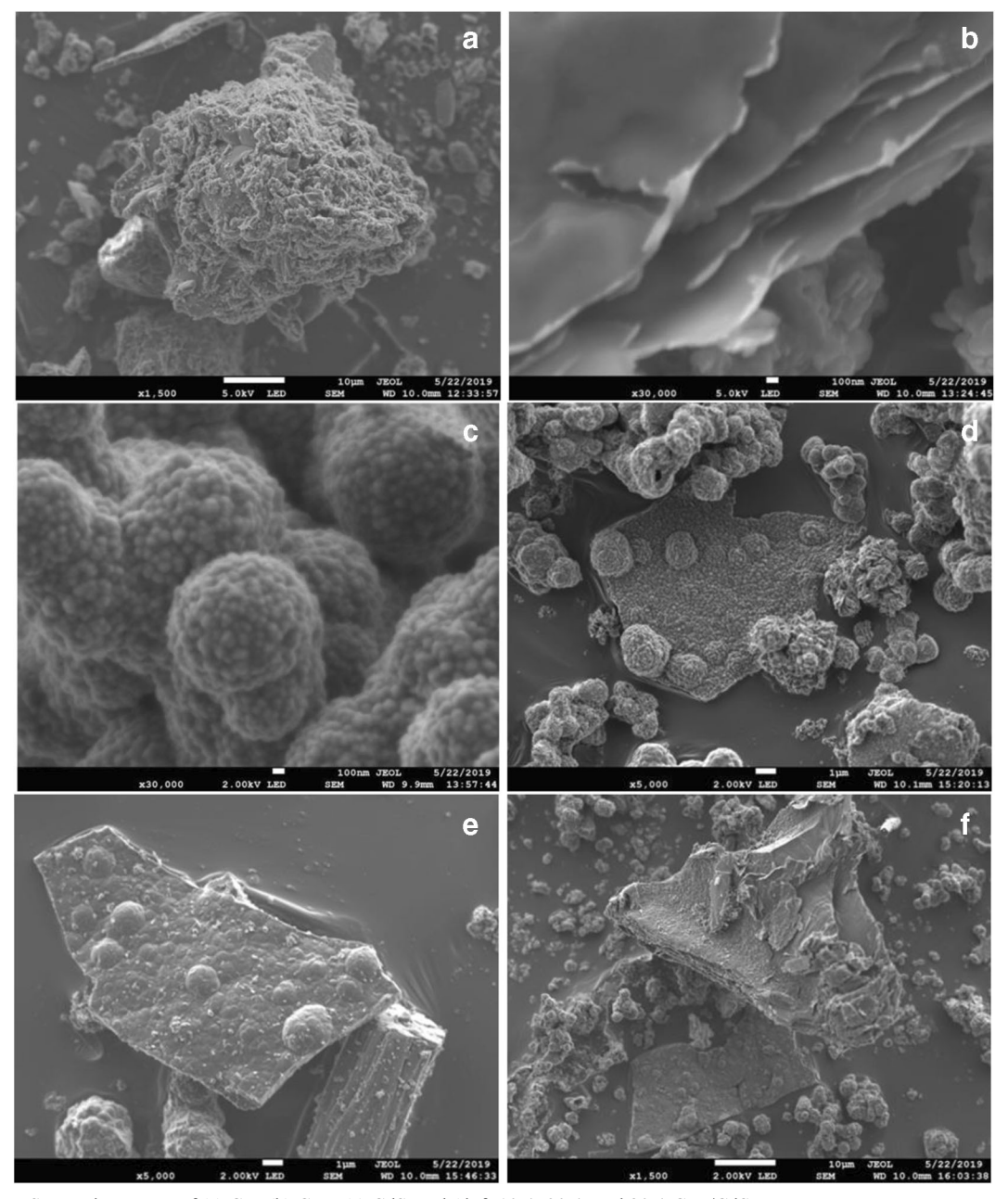


Fig. 3 FESEM micrograms of (a) CN, (b) CNs, (c) CdS, and (d-f) 10%, 20%, and 30% CNs/CdS

were found to be 3.04, 11.0, 1.11, and 4.37 m^2 g^{-1} , respectively. Upon exfoliation of CN to CNs, there was a remarkable increase in BET surface area, which could be vital for capturing pollutant prior to the photodegradation process. When CdS was anchored on CNs, the specific surface area of CdS increased from 1.11 to 4.37 m^2 g^{-1} , while that of CNs was reduced due to the clogging of some spaces by CdS berry-like structures.

The pore volume was obtained using the Barrett-Joyner Halenda (BJH) method and the obtained results are highlighted in Table 2. It was noted again that the pore volume of CN also increased after exfoliation. The pore volume of CdS also increased as CNs was incorporated and this increase might be of a great importance in transporting photogenerated charges. The pore volumes of all the samples are (<2 nm), indicating the



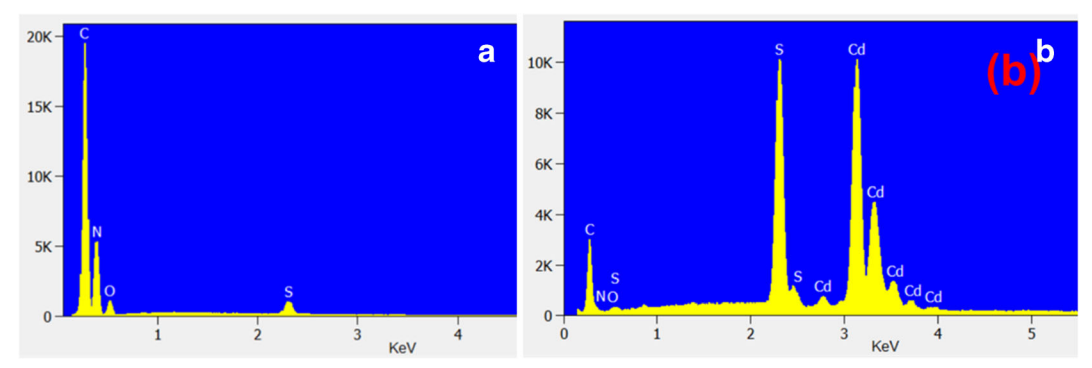


Fig. 4 EDS of (a) CNs and (b) 10% CNs/CdS

presence of microporous structure in the samples. Furthermore, higher pore volume resulted in increased

surface area of the sample, which could lead to enhanced photocatalytic activity.

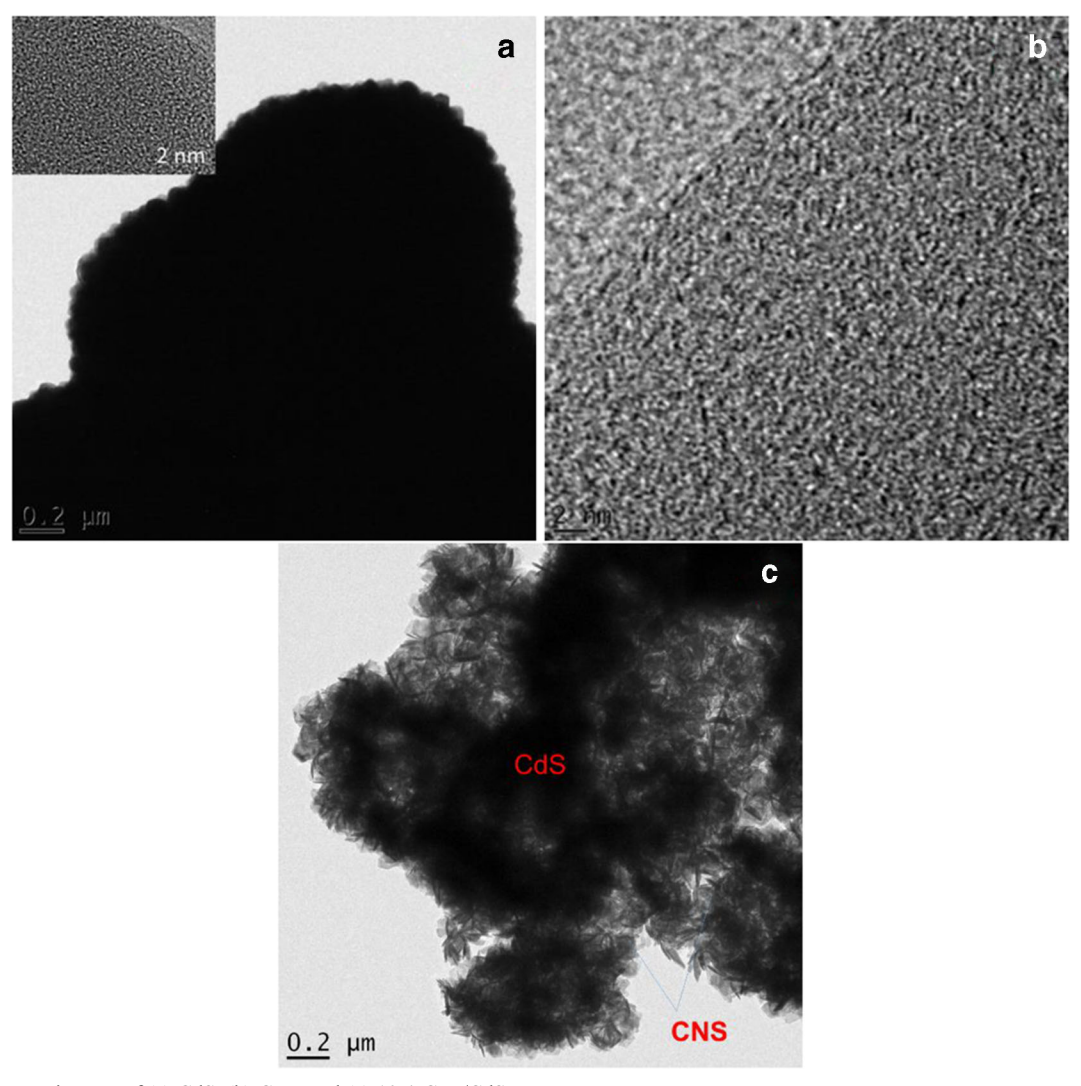


Fig. 5 TEM images of (a) CdS, (b) CNs, and (c) 10% CNs/CdS

16 Page 8 of 17 J Nanopart Res (2021) 23: 16

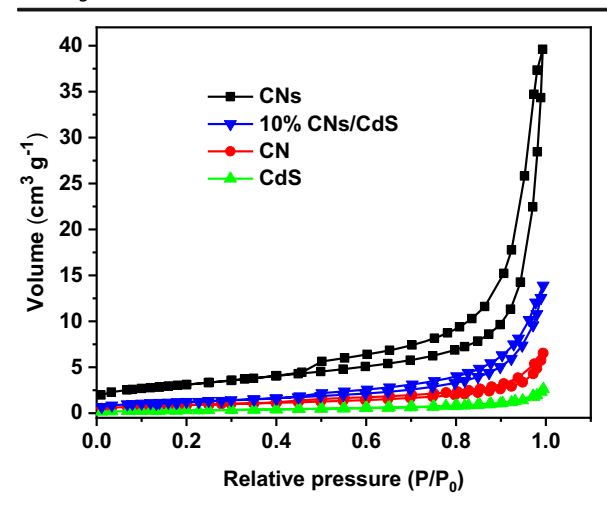


Fig. 6 BET analysis of the prepared materials

Optical properties

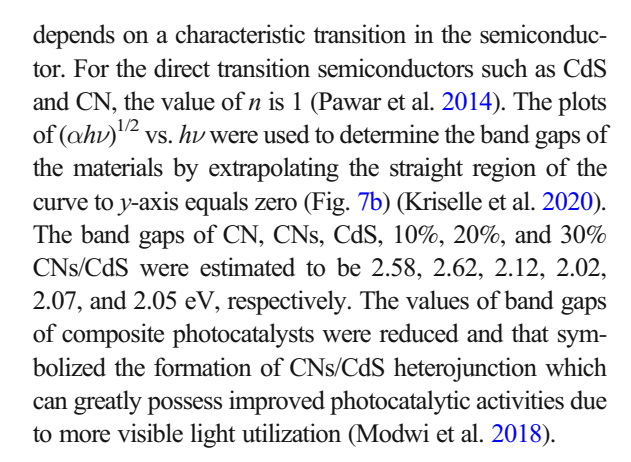
UV-Vis diffusive reflectance spectroscopy was used to determine the optical properties of the prepared materials (Fig. 7a). The CN and CNs showed light absorption in both UV and visible light regions. After CN exfoliation into CNs, there was an improvement in visible light absorption from around 420 nm to 800 nm. The shift is due to the quantum confinement property associated with the single layer of CNs. Moreover, the light absorption of CdS was higher in the UV and visible region when compared to CN and CNs. After addition of CNs, the light absorption shifted from 250 nm to 550 nm and increased from around 580 nm to 800 nm. This is a plausible route to use more visible light energy by the composite catalysts and subsequently generate more electron-hole pairs. The band gaps of the materials were estimated using Eq. (4);

$$\alpha h v = A \left(h v - E_g \right)^{n/2} \tag{4}$$

where is the absorption coefficient, ν is the light frequency, h is the Planck's constant, A is a proportionality constant, E_g is the band gap energy, and n is the value that

Table 2 Surface area and pore volume of the prepared materials

Sample	Surface area (m ² g ⁻¹)	Pore volume (cm ³ g ⁻¹)
CN	3.04	0.0089
CNs	11.02	0.0531
CdS	1.11	0.0036
10% CNs/CdS	4.37	0.0194



Photoluminescence studies

The emission peaks of CN, CNs, CdS, and CNs/CdS (10% and 20%) were evaluated using PL analysis (Fig. 8a, b). The emission peak of CN is located at 463 nm and blue shifted to 434 nm for CNs and is consistent with UV-Vis absorption spectra (Fig. 8a). Furthermore, the PL emission intensity of CNs is lower than that of CN suggesting the CNs had a low rate of electronhole recombination (Zou et al. 2016; Tong et al. 2015; Zhang et al. 2013). On the other hand, the two emission peaks for CdS are observed at 542 nm and 445 nm, respectively (Fig. 8b). These are due to the excited and trapped luminescence, in which the emission peak at 542 nm is attributed to the electronic transition from the conduction band to an acceptor level due to the interstitial sulfur ion (Mercy et al. 2013). Furthermore, a reduced peak in 10% CNs/CdS is observed, and this could be a break-through to reduction of the recombination rate of photogenerated electron-hole pairs.

Photocatalytic decolourisation of acid blue 25

The photocatalytic decolourisation of AB-25 was monitored over predetermined time intervals at the wavelength of maximum absorption of the dye as shown in Fig. 9a. As observed, the UV-Vis absorbance of AB-25 decreased with an increasing reaction time and this indicated that indeed the concentration of the dye was decreasing. Figure 9b displays the decolourisation profiles of AB-25 dye on different catalysts. The photocatalytic decolourisation efficiency of the dye by the irradiated light was so insignificant showing that the dye was very stable without the presence of photocatalyst. With CN, the decolourisation obtained was 23.0% and increased to



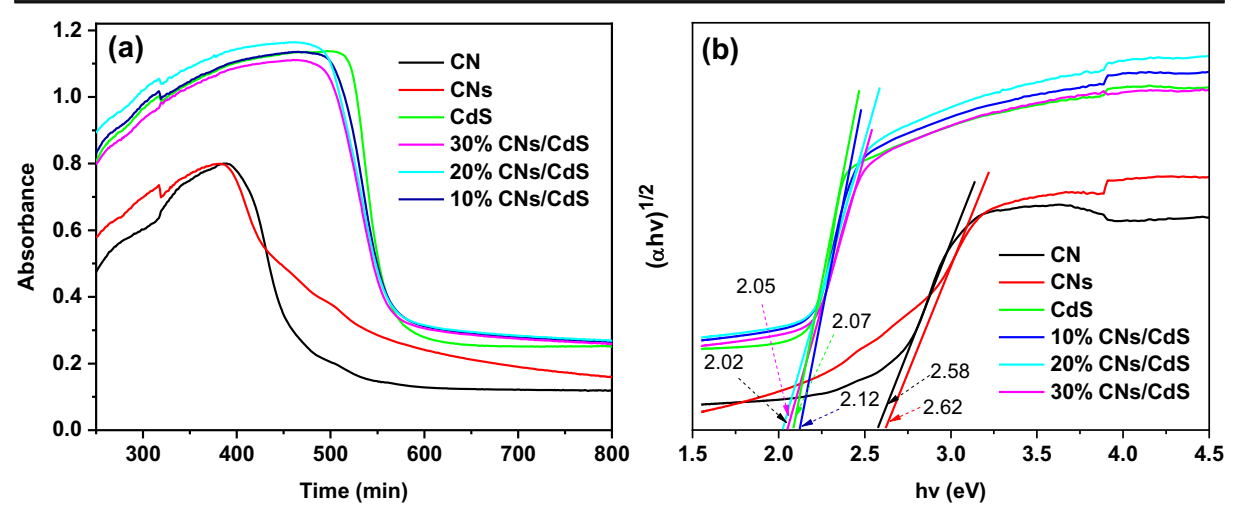


Fig. 7 (a) UV-Vis spectra and (b) Tauc plots of prepared materials

61.0% upon exfoliation. This enhanced decolourisation could be linked to high BET-specific surface area and improved visible light utilization. Moreover, the decolourisation displayed by CdS was 89.1%. When CNs and CdS were formed into 10%, 20%, and 30% CNs/CdS, the photocatalytic decolourisation improved significantly. The removal of 99.3%, 97.8%, and 92.1% was obtained for 10% CNs/CdS, 20% CNs/CdS, and 30% CNs/CdS, respectively. However, the increase from 10% to 20% and 30% was detrimental as the AB-25 removal was decreased (Oliveros et al. 2021). The composite with lower CNs content (10% CNs/CdS) exhibited higher dye removal which could be attributed to an intact heterojunction interface as shown by FESEM results, more visible light absorption and utilization, and low rate of

electron-hole recombination as depicted by the photoluminescence results. The high CNs content could have covered the active sites on the surface of CdS, therefore reducing the photocatalytic process (Fu et al. 2013; Tang et al. 2016). Furthermore, the decolourisation by 10% CNs/CdS evaluated by varying different parameters such as catalyst concentration, dye concentration, and pH of the dye solution as discussed in the subsequent sections.

Effect of catalyst dosage

Different amounts of catalyst were used for decolourisation of AB-25 to evaluate the optimum catalyst amount for best performance (Fig. 9c). The percentage decolouration for 20, 30, and 40 mg catalyst

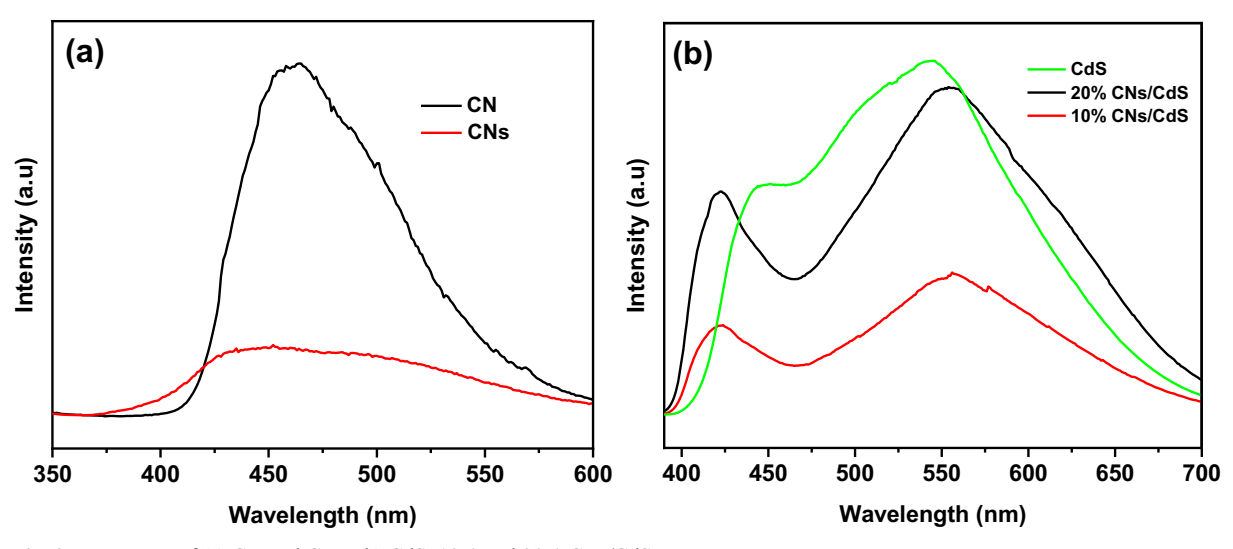


Fig. 8 PL spectra of (a) CN and CNs, (b) CdS, 10% and 20% CNs/CdS



16 Page 10 of 17 J Nanopart Res (2021) 23: 16

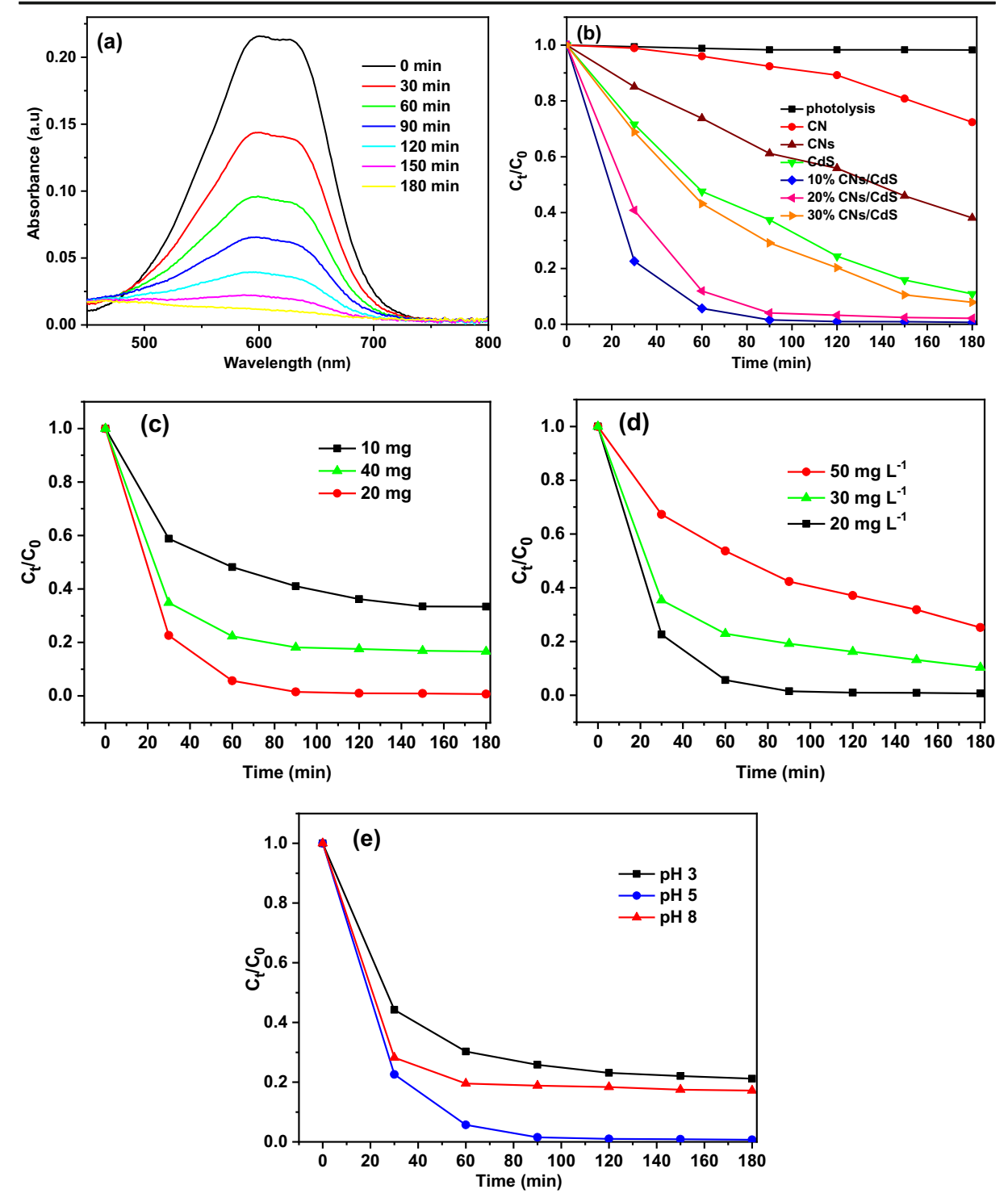


Fig. 9 (a) UV-Vis absorption spectra for decolourisation of AB-25, (b) AB-25 decolourisation on pristine and composite catalysts, (c) effect of CNs/CdS dosage, (d) effect of AB-25 concentration, and (e) effect of solution pH

were 99.3%, 89.6%, and 66.5%, respectively. The results show that when 10 mg was used for photocatalytic

decolourisation of AB-25, there were enough active sites on the catalyst surface to take part in the



decolourisation process (Wang et al. 2016). At higher catalyst dosage, the photocatalytic removal decreased, suggesting that there was poor light penetration through the slurry solution and may be aggravated by the coalescence of nanoparticles forming larger agglomerates which reduce the active surface area. This results in excessive light blockage and scattering by the photocatalyst particles which result in a decreased production of oxygen reactive species which take part in the decolourisation of the dye solution (Kumar 2017).

Effect of dye concentration

Different concentrations of AB-25 dye were selected based on the literature textile dye effluents discharge, which are reported in the range $20-50 \text{ mg L}^{-1}$ (Ananthashankar 2012). For initial dye concentrations of 20, 30, and 50 mg L⁻¹, the obtained percentage decolourisation was 99.3%, 89.5%, and 74.8%, respectively (Fig. 9d). Higher dye concentrations resulted in lower photocatalytic dye removal, suggesting there were more dye molecules to be accommodated by the catalyst active sites for the decolourisation process. Also, it was noted that at low concentrations the dye tends to block the light penetration towards the surface of the catalyst (Mafa et al. 2019a). Therefore, higher dye concentration was not ideal for the photocatalytic process as it was shielding light absorption by the catalyst and thus reducing production of active species.

Effect of pH

The pH of the dye solution is important in the adsorption process of dye, as it affects the overall charge on the dye molecules and surface of the catalyst (Han et al. 2014). Different pH values (3, 5, and 8) of dye solution were selected to evaluate the effect of pH of the solution on the process of photocatalytic decolourisation of AB-25. At low pH of 3, the photocatalytic removal of the dye was 78.8% while 99.3% and 82.8% were obtained for pH of 5 and 8, respectively. At the low pH (addition of HCl), there was a scavenging effect of chlorine ions in which it reacted with hydroxyl radicals to produce perchlorate radicals that can combine further with protons to yield weak oxidizing chlorine radicals (Malefane et al. 2019). As the pH was increased to 5, there was an enhanced photocatalytic decolourisation of AB-25. This could probably be linked to the effect of protonation of negatively charged sulfonic group (-SO₃⁻) which could have enhanced an electrostatic interaction between the dye and catalyst (Ghodbane and Hamdaoui 2010). As pH was further increased to 8, there was an observable decline in decolourisation of AB-25. There were more hydroxyl ions on the surface of the dye and some of them can abstract protons from the dye leaving it negatively charged. So the negatively charged dye and catalyst surface were repelling each other, thus, reducing the photocatalytic decolourisation of the dye. The results indicate that effective decolourisation of AB-25 by 10% CNs/CdS is feasible when the pH values are slightly acidic and neutral.

Reaction kinetics

The decolourisation rate of AB-25 was evaluated by modeling the decolourisation data using the Langmuir-Hinshelwood first-order kinetics using expression (5);

$$r = -dC/dt = \kappa_r KC/(1 + KC) \tag{5}$$

where κ_r is the reaction rate constant and K is the equilibrium coefficient. When $K \ll 1$, the concentration of the analyte is low owing to the process of dilution, and thus the reaction kinetics become pseudo-first order where $k_{\rm app}$ is the reaction rate constant (Eq. (6));

$$\ln C_0/C_t = \kappa_r K t = kt \tag{6}$$

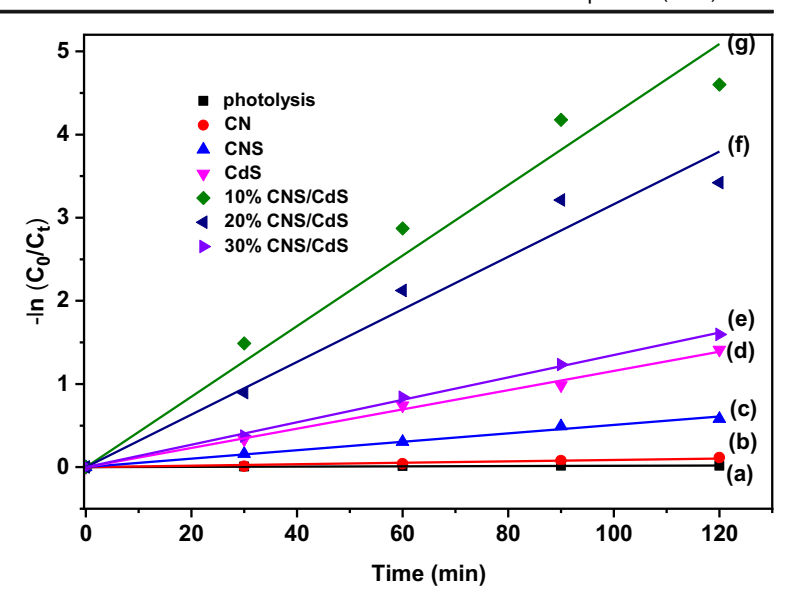
where C_0 and C_t are the concentrations of AB-25 at reaction time t. The apparent rate constant is determined from the slopes of $\ln C_0/C_t$ vs. t graphs and the slope is the rate of photocatalytic decolourisation (min⁻¹). The higher the reaction rate, the faster the reaction (Fig. 10). The rate constants for the different catalysts were obtained after fitting the data points and they are given in Table 3. The rate of photolysis was very low and very negligible. The photocatalytic rate of 10% CNs/CdS on decolourisation of AB-25 was the highest, and it was 8.3 and 3.7 folds higher than that of CNs and CdS, respectively. In general, the composite catalysts displayed higher rates than the pristine materials.

The high rates observed with composites, specifically the 10% CNs/CdS, could be attributed to the solid interface formed between the two materials that reduced the rate of electron-hole pair recombination and promoted visible light absorption which could help in the generation of more reactive radicals.



16 Page 12 of 17 J Nanopart Res (2021) 23: 16

Fig. 10 Rate constants for (a) photolysis, (b) CN, (c) CNs, (d) CdS, (e) 30% CNs/CdS, (f) 20% CNs/CdS, and (g) 10% CNs/CdS



Photocatalytic stability and reusability

The photocatalytic stability and reusability of the synthesized materials were evaluated by performing recyclability tests for 4 cycles. This is important for the real large-scale application of the CNs/CdS catalyst. After the completion of each catalytic cycle, the catalyst slurry was centrifuged, washed, and dried at 60 °C for 6 h prior to a subsequent cycle. The percentage decolourisation of AB-25 on CNs/CdS was found to be 99.3%, 97.8%, 94.5%, and 92.1% for the 1st, 2nd, 3rd, and 4th catalytic cycles, respectively (Fig. 11). As per the results obtained, the catalyst was still stable even after the 4th cycle and the reduction of 7.2% was recorded after the 4th cycle. The minor reduction in removal rate was ascribed to various factors such as partial blockage of active sites by the dye molecules and also the loss of the catalyst during the recovery steps.

Table 3 Reaction rate constants

Sample	Reaction rates (×10 ⁻³ min ⁻¹)
Photolysis	0.70
CN	0.90
CNs	5.10
CdS	11.6
10% CNs/CdS	42.4
20% CNs/CdS	31.6
30% CNs/CdS	13.5

Reactive species

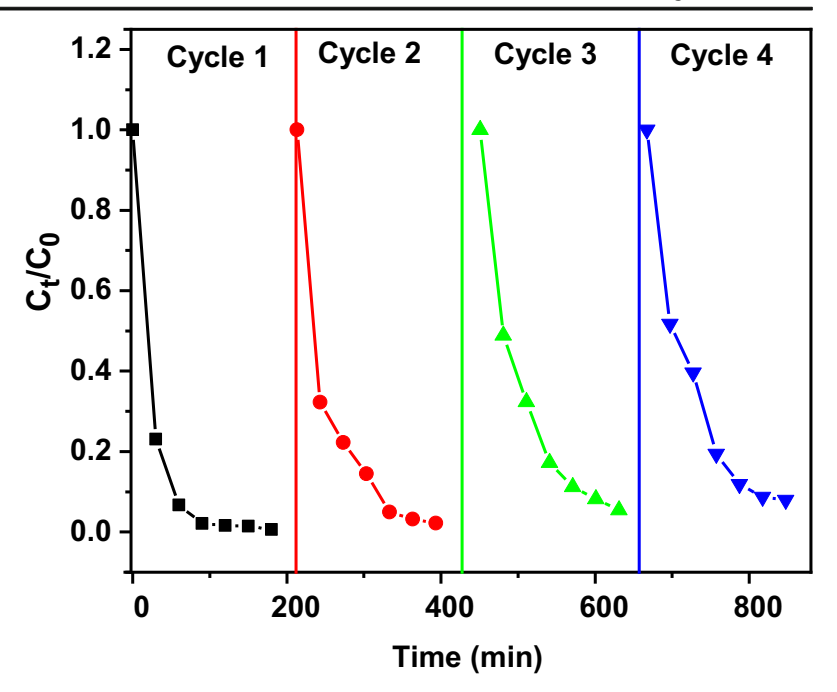
The charge carrier trapping experiments were conducted to determine the most reactive species in the photocatalytic decolourisation of AB-25 (Fig. 12). The radical scavengers such as benzoquinone (BQ), 2-propanol, and ethylenediamine tetraacetic acid disodium salt (EDTA-2Na) were used to evaluate their effects on superoxide radical anions (O₂•), hydroxyl radicals (HO•), and holes (h⁺) under optimum conditions (Mafa et al. 2020a). The addition of BQ, 2-propanol, and EDTA-2Na resulted in the decrease in the percentage decolourisation of AB-25 to 36.5%, 93.5%, and 85.6% respectively. It can be noted that the addition of 2-propanol showed minimal change on the photocatalytic decolourisation of AB-25 and that suggested that the HO^o radicals played a minor role. This was followed by EDTA-2Na showing the second minimal scavenging effects on the holes while the addition of BQ confirmed that $O_2^{\bullet-}$ was the major player in photocatalytic decolourisation of AB-25. The results indicate that the order of participation of reactive species was $O_2^{\bullet -} > h^+ > HO^{\bullet}$, respectively.

Photocatalytic mechanism

The proposed mechanism for the charge transfer and separation at the interface of the CNs/CdS during photocatalytic decolourisation AB-25 is depicted as a schematic diagram shown in Fig.13. In order to determine the separation of charges, the band edge potentials of the



Fig. 11 Photocatalytic stability of 10% CNs/CdS



conduction band (CB) and valence band (VB) of CNs and CdS were determined using Eqs. (7) and (8);

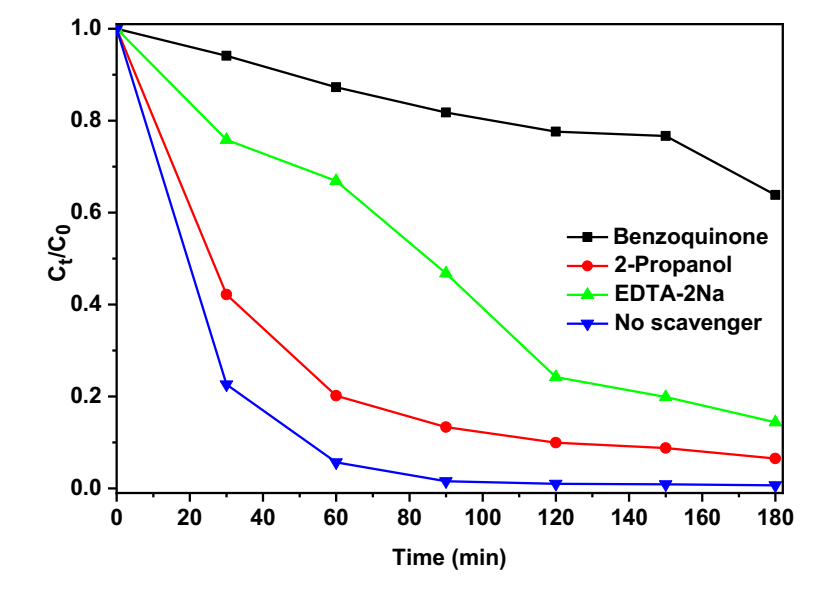
$$E_{\rm VB} = \chi - E^e + 0.5E_g \tag{7}$$

$$E_{\rm CB} = E_{\rm VB} - E_{\rm g} \tag{8}$$

where X is the electronegativity, which is the geometric mean of the electronegativity of the constituent atoms, E^e is the energy of the free electrons on the hydrogen

scale (approx. 4.5 eV), E_g is the bandgap energy of the semiconductor, $E_{\rm CB}$ and $E_{\rm VB}$ are the CB and VB potentials respectively (Mafa et al. 2019b). The electronegative values of CNs and CdS were calculated to be 4.74 eV and 5.14 eV, while their band gaps were found to be 2.62 eV and 2.12 eV, respectively. Accordingly, the conduction band (CB) and valence band (VB) potential of CNs were found to be -1.07 eV and 1.55 eV, while those of CdS were -0.32 eV and 1.70 eV,

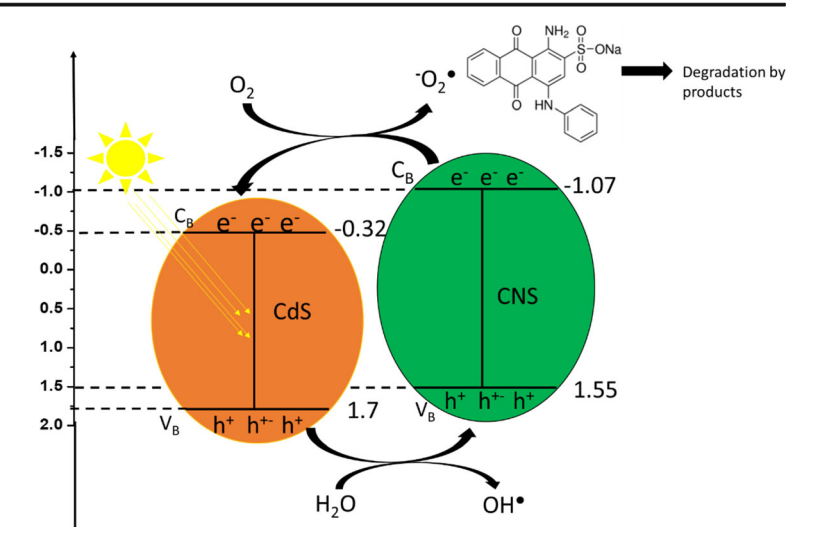
Fig. 12 Determination of reactive species with different scavengers for photodecolourisation of AB-25





16 Page 14 of 17 J Nanopart Res (2021) 23: 16

Fig. 13 The proposed mechanism for photocatalytic decolourisation of AB-25



respectively. During light illumination, both materials absorb photons and electrons are excited from their VB to their CB, leaving holes in VB. The CB of CNs is more negative than that of CdS; hence, electrons could travel from CB of CNs to that CdS and also reduce molecular oxygen (O2) into superoxide radicals (O2 •). This is because the potential of electrons from CNs is higher than the -0.33 eV vs. NHE of $O_2/(O_2^{\bullet-})$ couple (Han et al. 2020). On the other hand, the VB of CdS is more positive than that of CNs; hence, holes would migrate to VB of CdS to that of CNs where they will engage in oxidative reactions. In this way, the photo-generated electrons and holes move in opposite directions and thus reduce the chances of charge carrier recombination and enhance the charge separation efficiency. Separation of charges promotes generation of reactive radicals that participate in photocatalytic decolourisation of AB-25 the dye.

Conclusions

In summary, a photocatalyst composed of CNs and CdS was successfully synthesized using in situ hydrothermal method and was employed for the photocatalytic decolourisation of AB-25. The FESEM images showed that there was a contact formed between CNs and CdS berry-like structures. Among the composite catalyst prepared, 10% CNs/CdS heterojunction exhibited the highest photocatalytic decolourisation of AB-25 (99.3%),

which was 1.6 and 1.1 folds higher than that of CNs and CdS after 180 min of reaction. The enhanced activity was due to high visible light absorption and utilization and formation of the interface which enhanced separation of electronhole pairs. The optimum conditions were found to be 20 mg catalyst, 50 mL of 20 mg L⁻¹ of AB-25, and pH of 5. The results of trapping experiments indicated that the most active radicals were O₂• followed by h⁺ and HO• in that order. The photocatalyst that was prepared in this work was stable for 4 cycles, and this is a crucial property for real wastewater treatment applications.

Acknowledgments The authors would like to thank the department of physics (UNISA) for providing analysis facilities (FESEM, XRD, and PL), university of western cape also acknowledged and special thanks goes to the department of chemistry (UNISA) and the laboratory head Dr. Mkhize for providing space to carry out some of the experimental work.

Author's contribution M.P Sithole designed the project, lab work, and write up. P.M. Mafa did XRD analysis and revised the whole manuscript and responded to reviewers' comments. A.T. Kuvarega supervised the work. E. Viljoen and L.A. de Kock co-supervised the work.

Funding This work is funded by the Institute for Nanotechnology and Water Sustainability (iNanoWS) from the University of South Africa (UNISA) and National Research Foundation (NRF) (Grant no: 116370).

Compliance with ethical standards

Conflict of interest The authors confirm no conflict of interest.



References

- Adeyemo AA, Adeoye IO, Bello OS (2012) Metal organic frameworks as adsorbents for dye adsorption: overview, prospects and future challenges. Toxicol Environ Chem 94:1846–1863. https://doi.org/10.1080/02772248.2012.744023
- R. Ananthashankar, Treatment of textile effluent containing reactive red 120 dye using advanced oxidation, 2012
- Baughman GL, Weber EJ (1994) Transformation of dyes and related compounds in anoxic sediment: kinetics and products. Environ Sci Technol 28:267–276. https://doi.org/10.1021/es00051a013
- Bremner DH, Molina R, Martínez F, Melero JA, Segura Y (2009)
 Degradation of phenolic aqueous solutions by high frequency sono-Fenton systems (US-Fe₂O₃/SBA-15-H₂O₂). Appl Catal B Environ 90:380–388. https://doi.org/10.1016/j.apcatb.2009.03.028
- Cao SW, Yuan YP, Fang J, Shahjamali MM, Boey FYC, Barber J, Joachim Loo SC, Xue C (2013) In-situ growth of CdS quantum dots on g-C₃N₄ nanosheets for highly efficient photocatalytic hydrogen generation under visible light irradiation. Int J Hydrog Energy 38:1258–1266. https://doi. org/10.1016/j.ijhydene.2012.10.116
- Caruso F, Shi X, Caruso RA, Susha A (2001) Hollow titania spheres from layered precursor deposition on sacrificial colloidal core particles. Adv Mater 13:740–744. https://doi. org/10.1002/1521-4095(200105)13:10<740::AID-ADMA740>3.0.CO;2-6
- Cote LJ, Kim F, Huang J (2009) Langmuir-Blodgett assembly of graphite oxide single layers. J Am Chem Soc 131:1043– 1049. https://doi.org/10.1021/ja806262m
- Cui Y (2015) In-situ synthesis of C₃N₄/CdS composites with enhanced photocatalytic properties. Cuihua Xuebao/ Chinese J Catal 36:372–379. https://doi.org/10.1016/S1872-2067(14)60237-0
- Deka S, Falqui A, Pellegrino T, Morello G, Lupo MG, Lanzani G, Spinella C, Manna L, Cingolani R, Quarta A, De Giorgi M, Giannini C, Boninelli S (2009) CdSe/CdS/ZnS double shell nanorods with high photoluminescence efficiency and their exploitation as biolabeling probes. J Am Chem Soc 131: 2948–2958. https://doi.org/10.1021/ja808369e
- El-Hadi AM, Alamri HR (2018) The new generation from biomembrane with green technologies for wastewater treatment. Polymers (Basel) 10:1174. https://doi.org/10.3390/polym10101174
- Fischer A, Carlsson JM, Schlögl R, Antonietti M, Goettmann F, Thomas A, Müller J-O (2008) Graphitic carbon nitride materials: variation of structure and morphology and their use as metal-free catalysts. J Mater Chem 18:4893. https://doi. org/10.1039/b800274f
- Fu J, Chang B, Tian Y, Xi F, Dong X (2013) Novel C₃N₄-CdS composite photocatalysts with organic-inorganic heterojunctions: in situ synthesis, exceptional activity, high stability and photocatalytic mechanism. J Mater Chem A 1: 3083–3090. https://doi.org/10.1039/c2ta00672c
- Ganesh RS, Sharma SK, Durgadevi E, Navaneethan M, Binitha HS, Ponnusamy S, Muthamizhchelvan C, Hayakawa Y, Kim DY (2017) Surfactant free synthesis of CdS nanospheres, microstructural analysis, chemical bonding, optical

- properties and photocatalytic activities. Superlattice Microst 104:247–257. https://doi.org/10.1016/j.spmi.2017.02.029
- Ghodbane H, Hamdaoui O (2010) Decolorization of antraquinonic dye, C.I. acid blue 25, in aqueous solution by direct UV irradiation, UV/H₂O₂ and UV/Fe(II) processes. Chem Eng J 160:226–231. https://doi.org/10.1016/j.cej.2010.03.049
- Han ZX, Zhu Z, Wu DD, Wu J, Liu YR (2014) Adsorption kinetics and thermodynamics of acid blue 25 and methylene blue dye solutions on natural sepiolite. Synth React Inorganic, Met Nano-Metal Chem 44:140–147. https://doi. org/10.1080/15533174.2013.770755
- Han N, Xu Q, Beyene G, Zhang Q (2020) Enhanced photocatalytic activity over g- $C_3N_4/(BiO)2(OH)_xCl_{2-x}$ Z-scheme heterojunction. Appl Surf Sci 521:146464. https://doi.org/10.1016/j.apsusc.2020.146464
- Jiang F, Yan T, Chen H, Sun A, Xu C, Wang X (2014) A g-C₃N₄ CdS composite catalyst with high visible-light-driven catalytic activity and photostability for methylene blue degradation. Appl Surf Sci 295:164–172. https://doi.org/10.1016/j.apsusc.2014.01.022
- Kojima Y, Ohfuji H (2018) Reexamination of solvothermal synthesis of layered carbon nitride. J Mater 2018:1–8. https://doi.org/10.1155/2018/6576457
- Kriselle L, Paragas B, Dien Dang V, Shanker Sahu R, Garcia-Segura S, de Luna MDG, Pimentel JAI, Doong R-A (2020) Enhanced visible-light-driven photocatalytic degradation of acetaminophen over CeO₂/I, K-codoped C₃N₄ heterojunction with tunable properties in simulated water matrix. Sep Purif Technol 117567:117567. https://doi.org/10.1016/j.seppur.2020.117567
- Kumar A (2017) A review on the factors affecting the photocatalytic degradation of hazardous materials. Mater Sci Eng Int J 1:1–10. https://doi.org/10.15406/mseij.2017.01.00018
- Levchenko TI, Kübel C, Wang D, Khalili Najafabadi B, Huang Y, Corrigan JF (2015) Controlled solvothermal routes to hierarchical 3D superparticles of nanoscopic CdS. Chem Mater 27: 3666–3682. https://doi.org/10.1021/acs.chemmater.5b00586
- Li Q, Guo B, Yu J, Ran J, Zhang B, Yan H, Gong JR (2011a) Highly efficient visible-light-driven photocatalytic hydrogen production of CdS-cluster-decorated graphene nanosheets. J Am Chem Soc 133:10878–10884. https://doi.org/10.1021 /ja2025454
- Li Y, Bao J, Han M, Dai Z, Wang H (2011b) A simple assay to amplify the electrochemical signal by the aptamer based biosensor modified with CdS hollow nanospheres. Biosens Bioelectron 26:3531–3535. https://doi.org/10.1016/j.bios.2011.01.039
- Li G, Wang B, Zhang J, Wang R, Liu H (2019) Rational construction of a direct Z-scheme g-C₃N₄ /CdS photocatalyst with enhanced visible light photocatalytic activity and degradation of erythromycin and tetracycline. Appl Surf Sci 478:1056–1064. https://doi.org/10.1016/j.apsusc.2019.02.035
- Lin G, Zheng J, Xu R (2008) Template-free synthesis of uniform CdS hollow nanospheres and their photocatalytic activities. J Phys Chem C 112:7363–7370. https://doi.org/10.1021/jp8006969
- Litter MI (1999) Heterogeneous photocatalysis: transition metal ions in photocatalytic systems. Appl Catal B Environ 23:89–114. https://doi.org/10.1016/S0926-3373(99)00069-7
- Liu G, Li X, Zhao J, Hidaka H, Serpone N (2000) Photooxidation pathway of sulforhodamine-B. Dependence on the



16 Page 16 of 17 J Nanopart Res (2021) 23: 16

- adsorption mode on TiO₂ exposed to visible light radiation. Environ Sci Technol 34:3982–3990. https://doi.org/10.1021/es001064c
- Liu QY, Qi YL, Zheng YF, Song XC (2017) Synthesis and enhanced photocatalytic activity of g-C₃N₄ hybridized CdS nanoparticles. Bull Mater Sci 40:1329–1333. https://doi. org/10.1007/s12034-017-1513-y
- Lü J, Lin JX, Zhao XL, Cao R (2012) Photochromic hybrid materials of cucurbituril and polyoxometalates as photocatalysts under visible light. Chem Commun 48:669– 671. https://doi.org/10.1039/c1cc16268c
- Mafa PJ, Ntsendwana B, Mamba BB, Kuvarega AT (2019a) Visible light driven ZnMoO₄/BiFeWO₆/rGO Z-scheme photocatalyst for the degradation of Anthraquinonic dye. J Phys Chem C 123:20605–20616. https://doi.org/10.1021 /acs.jpcc.9b05008
- Mafa PJ, Kuvarega AT, Mamba BB, Ntsendwana B (2019b) Photoelectrocatalytic degradation of sulfamethoxazole on g-C₃N₄/BiOI/EG p-n heterojunction photoanode under visible light irradiation. Appl Surf Sci 483:506–520. https://doi.org/10.1016/j.apsusc.2019.03.281
- Mafa P, Mamba B, Kuvarega A (2020a) Construction of hierarchical BiPW₁₂O₄₀/BiOI p-n heterojunction with enhanced visible light activity for degradation of endocrine disrupting Bisphenol A. Sep Purif Technol 253:117349. https://doi.org/10.1016/j.seppur.2020.117349
- Mafa PJ, Mamba BB, Kuvarega AT (2020b) Photoelectrocatalytic evaluation of EG-CeO₂ photoanode on degradation of 2,4dichlorophenol. Sol Energy Mater Sol Cells 208:110416. https://doi.org/10.1016/j.solmat.2020.110416
- Malefane ME, Ntsendwana B, Mafa PJ, Mabuba N, Feleni U, Kuvarega AT (2019) In-situ synthesis of tetraphenylporphyrin/tungsten (VI) oxide/reduced graphene oxide (TPP/WO₃/RGO) nanocomposite for visible light photocatalytic degradation of acid blue 25. ChemistrySelect. 4: 8379–8389. https://doi.org/10.1002/slct.201901589
- Mercy A, Samuel Selvaraj R, Milton Boaz B, Anandhi A, Kanagadurai R (2013) Synthesis, structural and optical characterisation of cadmium sulphide nanoparticles. Indian J Pure Appl Phys 51:448–452
- Modwi A, Ghanem MA, Al-Mayouf AM, Houas A (2018) Lowering energy band gap and enhancing photocatalytic properties of Cu/ZnO composite decorated by transition metals. J Mol Struct 1173:1–6. https://doi.org/10.1016/j. molstruc.2018.06.082
- Oliveros AN, Pimentel JAI, de Luna MDG, Garcia-Segura S, Abarca RRM, Doong RA (2021) Visible-light photocatalytic diclofenac removal by tunable vanadium pentoxide/borondoped graphitic carbon nitride composite. Chem Eng J 403: 126213. https://doi.org/10.1016/j.cej.2020.126213
- Pal K, Yang X, Mohan MLNM, Schirhagl R, Wang G (2016) Switchable, self-assembled CdS nanomaterials embedded in liquid crystal cell for high performance static memory device. Mater Lett 169:37–41. https://doi.org/10.1016/j.matlet.2016.01.064
- Pawar RC, Khare V, Lee CS (2014) Hybrid photocatalysts using graphitic carbon nitride/cadmium sulfide/reduced graphene oxide (g-C₃N₄/CdS/RGO) for superior photodegradation of organic pollutants under UV and visible light. Dalton Trans 43:12514–12527. https://doi.org/10.1039/c4dt01278j

- Pietra F, Van Dijk-Moes RJA, Ke X, Bals S, Van Tendeloo G, Donega CDM, Vanmaekelbergh D (2013) Synthesis of highly luminescent silica-coated CdSe/CdS nanorods. Chem Mater 25:3427–3434. https://doi.org/10.1021/cm401169t
- Rengaraj S, Ferancova A, Jee SH, Venkataraj S, Kim Y, Labuda J, Sillanpää M (2010) Physical and electrochemical characterization of CdS hollow microspheres prepared by a novel template free solution phase method. Electrochim Acta 56: 501–509. https://doi.org/10.1016/j.electacta.2010.09.019
- Senker J, Schwinghammer K, Lotsch BV, Ziegler C, Mesch MB, Duppel V (2014) Crystalline carbon nitride nanosheets for improved visible-light hydrogen evolution. J Am Chem Soc 136:1730–1733. https://doi.org/10.1021/ja411321s
- Tang Q, Zhou C, Yuan X, Jing Q, Mu Y, Du A (2016) Facile synthesis of g-C₃N₄ nanosheets/ZnO nanocomposites with enhanced photocatalytic activity in reduction of aqueous chromium(VI) under visible light. Nanomaterials. 6:173. https://doi.org/10.3390/nano6090173
- Thompson TL, Yates JT (2006) Surface science studies of the photoactivation of TiO₂ new photochemical processes. Chem Rev 106:4428–4453. https://doi.org/10.1021/cr050172k
- Tong J, Zhang L, Li F, Wang K, Han L, Cao S (2015) Rapid and high-yield production of g-C₃N₄ nanosheets via chemical exfoliation for photocatalytic H₂ evolution. RSC Adv 5: 88149–88153. https://doi.org/10.1039/c5ra16988g
- Vadivel S, Maruthamani D, Paul B, Dhar SS, Selvam K (2016) Facile synthesis of novel CaFe₂O₄/g-C₃N₄ nanocomposites for degradation of methylene blue under visible-light irradiation. J Colloid Interface Sci 480:126–136. https://doi.org/10.1016/j.jcis.2016.07.012
- Wang X, Blechert S, Antonietti M (2012) Polymeric graphitic carbon nitride for heterogeneous photocatalysis. ACS Catal 2:1596–1606. https://doi.org/10.1021/cs300240x
- Wang CC, Li JR, Lv XL, Zhang YQ, Guo G (2014) Photocatalytic organic pollutants degradation in metal-organic frameworks. Energy Environ Sci 7:2831–2867. https://doi.org/10.1039/c4 ee01299b
- Wang M, Wu Z, Dai L (2015) Graphitic carbon nitrides supported by nitrogen-doped graphene as efficient metal-free electrocatalysts for oxygen reduction. J Electroanal Chem 753:16–20. https://doi.org/10.1016/j.jelechem.2015.05.012
- Wang D, Xu Z, Luo Q, Li X, An J, Yin R, Bao C (2016)
 Preparation and visible-light photocatalytic performances of
 g-C₃N₄ surface hybridized with a small amount of CdS
 nanoparticles. J Mater Sci 51:893–902. https://doi.
 org/10.1007/s10853-015-9417-y
- Wu W, Liu G, Xie Q, Liang S, Zheng H, Yuan R, Su W, Wu L (2012) A simple and highly efficient route for the preparation of p-phenylenediamine by reducing 4-nitroaniline over commercial CdS visible light-driven photocatalyst in water. Green Chem 14:1705–1709. https://doi.org/10.1039/c2 gc35231a
- Xie Y, Zhang X, Pan B, Xie X, Zhang J, Wang H (2012) Enhanced photoresponsive ultrathin graphitic-phase C3N4 nanosheets for bioimaging. J Am Chem Soc 135:18–21. https://doi.org/10.1021/ja308249k
- Xu J, Zhang L, Shi R, Zhu Y (2013) Chemical exfoliation of graphitic carbon nitride for efficient heterogeneous photocatalysis. J Mater Chem A 1:14766-14772. https://doi.org/10.1039/c3ta13188b



Yao WT, Yu SH, Liu SJ, Chen JP, Liu XM, Li FQ (2006) Architectural control syntheses of CdS and CdSe nanoflowers, branched nanowires, and nanotrees via a solvothermal approach in a mixed solution and their photocatalytic property. J Phys Chem B 110:11704–11710. https://doi.org/10.1021/jp060164n

- Zhang X, Xie X, Wang H, Zhang J, Pan B, Xie Y (2013) Enhanced photoresponsive ultrathin graphitic-phase C₃N₄ nanosheets for bioimaging. J Am Chem Soc 135:18–21. https://doi.org/10.1021/ja308249k
- Zhou Z, Wang J, Yu J, Shen Y, Li Y, Liu A, Liu S, Zhang Y (2015) Dissolution and liquid crystals phase of 2D polymeric

- carbon nitride. J Am Chem Soc 137:2179–2182. https://doi.org/10.1021/ja512179x
- Zou LR, Huang GF, Li DF, Liu JH, Pan AL, Huang WQ (2016) A facile and rapid route for synthesis of g-C₃N₄ nanosheets with high adsorption capacity and photocatalytic activity. RSC Adv 6:86688–86694. https://doi.org/10.1039/c6 ra20514c

Publisher's note Springer Nature remains neutral with regard to jurisdictional claims in published maps and institutional affiliations.



Journal of Nanoparticle Research is a copyright of Springer, 2021. All Rights Reserved.